

Supplementary Material to

“Climate Sensitivity Estimated From Temperature Reconstructions of the Last Glacial Maximum” by Schmittner, A., N. M. Urban, J. D. Shakun, N. D. Mahowald, P. U. Clark, P. J. Bartlein, A. C. Mix, and A. Rosell-Melé (2011) *Science*

Contents:

1. Climate Model, Radiative Forcing and Ensemble Generation

2. Temperature Reconstructions

3. Snowball Earth

4. Simulated Ocean Circulation

5. Data-Model Comparisons and Residual Analysis

6. Statistical Analysis

7. Sensitivity Tests

8. Vegetation Simulation

1. Climate Model, Radiative Forcing and Ensemble Generation

The UVic Earth System Climate Model (version 2.8 with parameters as described in detail in [Schmittner *et al.*, 2008]) includes a three-dimensional ocean general circulation model, a dynamic-thermodynamic sea ice model, a simple one-layer energy-moisture balance model of the atmosphere as well as land-surface and dynamic terrestrial vegetation components at a resolution of $1.8^{\circ} \times 3.6^{\circ}$ with 19 vertical levels in the ocean. Since vegetation is allowed to

respond dynamically to changes in climate and CO₂ concentrations, it is treated as an internal interactive feedback, rather than as part of the prescribed forcing as in previous studies without interactive vegetation.

In order to generate model versions with different climate sensitivities we have changed a parameter in the formulation of outgoing planetary longwave radiation at the top-of-the-atmosphere Q_{PLW} in the atmospheric Energy-Moisture Balance Model (EMBM) of the UVic model version 2.8 [Weaver *et al.*, 2001; Schmittner *et al.*, 2008]. The UVic model uses a polynomial formulation by Thompson and Warren (1982):

$$Q_{PLW} = c_{00} + c_{01}r + c_{02}r^2 + (c_{10} + c_{11}r + c_{12}r^2)T_a + (c_{20} + c_{21}r + c_{22}r^2)T_a^2 + (c_{30} + c_{31}r + c_{32}r^2)T_a^3 \quad (S1)$$

that depends on surface air temperature T_a and surface relative humidity r . In order to keep global preindustrial surface air temperature constant we varied the slope of this curve with respect to T_a by changing c_{10} and c_{00} simultaneously (Figure S1). Equation S1 implicitly includes the effects of the water vapor and lapse-rate feedbacks as well as cloud feedbacks on infrared radiation. The larger the slope c_{10} the larger the response of Q_{PLW} will be to a given change in temperature. Since this is a negative feedback, the climate sensitivity is smaller the larger the slope c_{10} . We have created an ensemble of 26 different model versions by varying c_{10} from 1.7 to 18.1 Wm⁻²K⁻¹. The standard model uses $c_{10} = 2.6$ Wm⁻²K⁻¹. Present-day observations do not provide firm constraints on these parameters as illustrated in Figure S1, although very small and very large values can probably be excluded. However, we have retained models with extreme values in order to gauge the constraints imposed by LGM data only, without considering

constraints from present day observations.

We carried out three types of simulations with each ensemble member: a pre-industrial control run, a double CO₂ run (to determine ECS_{2xC}) and four LGM experiments. The LGM experiments consider uncertainty in dust forcing, wind stress and initial conditions (different initial states of the Atlantic Meridional Overturning Circulation AMOC). All simulations were integrated for 2000 years after which surface climate is close to equilibrium. (E.g. global mean surface air temperature changes by 2.2×10^{-4} K/yr for $ECS_{2xC}=5.6$). The average of the last 500 years were used for the analysis.

Our standard model simulations of the Last Glacial Maximum (LGM) include radiative forcing from larger continental ice sheets ($\Delta F_{sfc} = -2.2$ W/m²) [Peltier, 2004], lower greenhouse gas concentrations (CO₂, CH₄, N₂O) ($\Delta F_{GHG} = \Delta F_{CO_2} + \Delta F_{CH_4} + \Delta F_{N_2O} = -2.8$ W/m²) [Flückiger et al., 1999; Ramaswamy et al., 2001; EPICA et al., 2004], changes in the seasonal distribution of insolation (annually averaged $\Delta F_{ins} = 0$ W/m²), and higher atmospheric dust levels (Figure S2; $\Delta F_{dust} = -0.9$ W/m²) [Mahowald et al., 2006b]. The total radiative forcing in the standard model $\Delta F_{LGM} = \Delta F_{sfc} + \Delta F_{GHG} + \Delta F_{dust} = -5.9$ W/m² is similar to previous estimates [Hansen et al., 1984], but less than another recent study [Köhler et al., 2010] who estimated $\Delta F_{LGM} = -9.5$ W/m², partly because of higher assumed dust $\Delta F_{dust} = -1.9$ W/m² and ice sheet $\Delta F_{sfc} = -3.2$ W/m² forcing by Köhler et al. and because they prescribe surface albedo changed from changes in vegetation $\Delta F_{veg} = -1.1$ W/m², which is considered an internal feedback in our study.

Our ensemble explores uncertainties in dust forcing by including simulations without dust, but it does not explore uncertainties in surface or greenhouse gas forcings.

Ice sheets are prescribed as fixed differences in the surface elevation in the model (not interactive). This affects surface air temperatures according to a fixed lapse rate (5K/km), which leads to a changed albedo because of accumulating snow cover. (Albedo is not prescribed.) Forcing due to surface albedo changes associated with the increased land area covered with ice sheets was estimated by performing an additional simulation with pre-industrial boundary conditions but added LGM ice sheets. The difference in shortwave fluxes at the top of the atmosphere between this experiment and the pre-industrial control run gives the forcing due to surface albedo changes resulting in the value of $\Delta F_{sfc} = -2.2 \text{ W/m}^2$ reported above. Northern hemisphere ice sheets contribute -1.8 W/m^2 , southern hemisphere ice sheets -0.3 W/m^2 and changes in non-ice sheet covered areas -0.1 W/m^2 . This estimate, which includes the effects of changes in snow cover, is within the range (-1.9 to -2.9 W/m^2) of previous studies [Hewitt and Mitchell, 1997; Broccoli, 2000; Taylor et al., 2007] but smaller than the -3.2 W/m^2 by Köhler et al. [2010]. We do not consider the effect of surface albedo changes caused by differences in land-sea distribution away from ice sheets associated with exposed continental shelves. This effect has been estimated to be small (-0.4 W/m^2) [Broccoli, 2000]. Including this forcing, which is 7% of the total, could decrease our estimate of ECS_{2xC} slightly (by up to 0.2 K).

For dust we use two-dimensional maps (Figure S2) of longwave and shortwave radiative forcing for the LGM and pre-industrial climate as simulated by the interactive dust model of [Mahowald et al., 2006b], which uses the Community Atmospheric Model, as described in [Mahowald et al., 2006a]. The dust model results were tuned for the LGM to best match available deposition observations, and matched these observations for the current climate, especially in the annual mean. The shortwave and longwave impacts of desert dust were included, as described in [Yoshioka et al., 2007]. We assumed the best available optical values

for the desert dust particles [Yoshioka *et al.*, 2007], but these are uncertain [Sokolik and Toon, 1999], and there are large differences in the results if different optical values are used [Perlwitz *et al.*, 2001].

2. Temperature Reconstructions

We have combined recent syntheses of global sea surface temperatures (SSTs) from the Multiproxy Approach for the Reconstruction of the Glacial Ocean (MARGO) project [MARGO *et al.*, 2009] and surface air temperatures (SAT) over land based on pollen distributions [Bartlein *et al.*, 2011], with additional data (see subsection 2.1 below) from ice sheets, land and ocean [Shakun *et al.*, 2011]. The combined temperature reconstructions are shown in Figure 1. The published error estimates are shown in Figure S3.

2.1. Shakun *et al.* (submitted) LGM temperature dataset

This dataset consists of 54 proxy temperature records spanning some or the entire LGM interval (19-23 ka) that are not included in the MARGO (2009) or Bartlein *et al.* (2011) datasets. The records are based on various proxies from ocean, land, and ice, including alkenones (n=21), foraminiferal Mg/Ca (n=18), foraminiferal assemblages (n=4), TEX₈₆ (n=4), MBT/CBT (n=2), and ice cores (n=5). LGM temperature anomalies and errors were calculated following the methods used by MARGO (2009). One difference, however, is that many of these records (n=34) are high-resolution time series that extend to the late Holocene. Therefore, LGM anomalies for these records were calculated as the difference between the 19-23 ka and 0-2 ka means. This approach only assumes that the proxies accurately record the magnitude of LGM-Late Holocene temperature change, rather than absolute LGM temperatures. For the remaining 20 records, LGM

anomalies were calculated from modern mean annual temperature at 10 m water depth using the World Ocean Atlas 98 dataset, as done by MARGO (2009). Twenty-six of the ocean records come from locations where the MARGO 5°x5° LGM temperature anomaly grid already contains values. Therefore, these MARGO grid points were updated with these new records, and errors were propagated following MARGO's (2009) methods. The dataset is available at <http://mgg.coas.oregonstate.edu/~andreas/data/schmittner11sci/>.

2.2 Mg/Ca salinity bias

Recent research suggests that foraminiferal Mg/Ca may be sensitive to salinity [Mathien-Blard and Bassinot, 2009; Arbuszewski et al., 2010]. If so, correcting Mg/Ca records for the ~1 unit increase in global ocean salinity at the LGM would decrease reconstructed SSTs. The magnitude of this temperature correction would vary with the absolute value of the salinity and SST at the core site due to the nonlinear relationships between salinity and “excess Mg/Ca”, and Mg/Ca and SST. For example, [Mathien-Blard and Bassinot, 2009] estimate an additional 1°C LGM cooling for a western tropical Pacific record, while [Arbuszewski et al., 2010] calculate an additional 1.8°C cooling for a Caribbean record. Since none of the Mg/Ca records used in our study have been corrected for this salinity effect, taking it into account would increase reconstructed LGM cooling and thus our estimate of climate sensitivity. Nonetheless, we estimate that the impact on our results would be minor. In particular, Mg/Ca accounts for only 9% (66 of 742) of the individual SST reconstructions used here, and only 5% of the global (ocean and land) temperature reconstructions. Moreover, it is unclear now many of these Mg/Ca reconstructions were affected by large salinity changes that would introduce a bias since it only occurs at high salinities (>35) [Arbuszewski et al., 2010]. Assuming a typical temperature correction of -1°C for all Mg/Ca records due to this salinity effect and averaging that through to

the LGM global cooling estimate would increase it on the order of $\sim 0.05^{\circ}\text{C}$ (i.e., 5% of 1°C). This is well within the error of our $3.6 \pm 1^{\circ}\text{C}$ LGM cooling estimate and would have little effect on the likely range of climate sensitivity we report.

The reconstructed LGM-modern temperature anomalies are plotted against the reconstruction errors in Figure S4. Land points show greater LGM cooling than ocean points. The SST proxies, however, generally have greater reconstruction errors than the land proxies.

3. Snowball Earth

Figure S5 shows three snapshots in the transition to a completely ice covered Earth for a high climate sensitivity model ($\text{ECS}_{2\times\text{C}} = 8.2 \text{ K}$). Shortly after model year 460, that is 460 years after the switch to LGM boundary conditions, Earth is completely ice covered in this simulation.

4. Simulated Ocean Circulation

For LGM boundary conditions the standard model exhibits a threshold around $\text{ECS}_{2\times\text{C}} = 2.7$ at which the Meridional Overturning Circulation (MOC) of the ocean changes from a mode with deep water formation in the North Atlantic ($\text{ECS}_{2\times\text{C}} < 2.7$) to a mode with deep water formation in the North Pacific ($\text{ECS}_{2\times\text{C}} > 2.7$) as illustrated in Figure S6. Note that only an index of the Atlantic MOC is shown in Figure S6, but inspection of the full streamfunction shows that the mode with zero AMOC exhibits sinking in the North Pacific down to about 2000 m depth (not shown) due to the Atlantic-Pacific seesaw mechanism [Saenko *et al.*, 2004], whereas the mode with active AMOC has no deep water formation in the North Pacific. The mode with deep water formation

in the North Atlantic is consistent with the observed modern circulation pattern whereas the mode with sinking in the North Pacific is not. Paleoclimate data show that deep water formation in the North Atlantic was active during the LGM (albeit perhaps weaker and/or shallower than at present day) [Curry and Oppo, 2005] contrary to the standard model results for high climate sensitivities. Sensitivity experiments with added wind stress anomalies from a coupled ocean-atmosphere model (GENMOM) [Alder et al., 2011] result in a stronger AMOC than that of the control simulation and do not exhibit the threshold seen in the model without wind stress anomalies. Results from these experiments show that the climate sensitivity estimates do not depend much on the state of the MOC (subsection 7.3).

5. Data-Model Comparisons and Residual Analysis

Figure S7 shows the zonally averaged temperature changes from the best fitting model ($ECS_{2xC}=2.4$ K), Figure S8 shows the spatial distribution of the residuals (model minus reconstructions). The correlation coefficient for the 2D temperature changes is 0.53 and the root mean squared error is 2.3 K.

Histograms of reconstructed temperature anomalies are plotted against the modeled temperature anomalies for several different climate sensitivities in Figure S9. The reconstructed SSTs are most compatible with a model ECS_{2xC} near 2 K, whereas the reconstructed land SATs are most compatible with a model ECS_{2xC} near 3 or 4 K, when comparing peaks of the reconstructed and modeled anomaly distributions. When land and ocean anomalies are considered together, an ECS_{2xC} near 2 K is favored when comparing peaks, similar to the SST

comparison, likely because the ocean data are more abundant than the land data.

The data-model residual temperature anomalies are plotted in Figure S10 for $ECS_{2xC} = 2.2$ K. The residuals show some evidence of non-normality. However, the land and ocean residuals individually appear more normal, suggesting that the combined residuals are a mixture of two normal distributions. This motivates a statistical treatment of the data as normally distributed with different covariance structures over land and ocean. The land residuals show greater variability than the ocean residuals, as might be expected. Neither the land nor ocean residuals display a strong skewness, nor particularly heavy tails. While the ocean residuals are centered at zero the land residuals are not, indicating that the land data do not favor this ECS_{2xC} value.

To further explore the differences between the ECS_{2xC} values implied by the land and ocean data, Figure S11 plots the mean and 90% interval of the reconstructed temperature anomalies against the mean and 90% interval of the modeled temperature anomalies as a function of model ECS_{2xC} . The range of modeled land SAT anomalies lies within the range of reconstructed SAT anomalies for ECS_{2xC} below ~ 5 K, whereas the range of modeled ocean SST anomalies lies within the range of reconstructed SST anomalies for ECS_{2xC} below ~ 3 K. This is compatible with the Figure S9, which shows that the ocean SST data favor lower ECS_{2xC} values than the land SAT data.

The modeled ocean anomalies also show an abrupt decrease in the lower temperature

range near $ECS_{2xC} = 2.7$ K, where the AMOC collapses (Fig. S6). Figure S12 shows a data model comparison with the North Atlantic points excluded. (The excluded region is defined empirically to be those Northern Hemisphere ocean grid cells for which the modeled temperature anomaly in the $ECS_{2xC} = 2.83$ K run is more than 1 K colder than the anomalies in the $ECS_{2xC} = 2.51$ K run. This includes most of the North Atlantic and Mediterranean Sea, and no other grid cells.) The data-model comparison suggests that SST data outside of the North Atlantic region are compatible with a larger range of climate sensitivities (below $ECS_{2xC} = 4$ K) than are the SST data with the AMOC region included (as discussed above).

6. Statistical Analysis

6.1 Regridding and Sea Level Correction

For the purpose of data-model comparison the model output is mapped from the UVic grid ($1.8 \times 3.6^\circ$) onto the grids of the temperature reconstructions ($5 \times 5^\circ$ grid for the SSTs and Shakun et al. data and $2 \times 2^\circ$ grid for the pollen data). A correction of 0.32 K is added to the modeled SST everywhere in order to account for the 120 m lower sea level at the LGM. The value of $\Delta SST_{SL} = 0.32$ K is determined from an additional model simulation in which sea level is explicitly lowered and a constant global mean lapse rate of 5 K km^{-1} is used to calculate surface air temperatures. The analysis uses modeled SSTs over the oceans and SATs over land.

6.2 Model Emulation

In order to predict the model output at arbitrary climate sensitivities, the model output at each grid cell is emulated by linear interpolation of the model output over the ECS_{2xC} values in the

ensemble. A total of $n=435$ independent linear emulators are constructed, one for each grid cell containing data. In addition to a linear interpolator, several other types of statistical emulators were also evaluated, including independent cubic spline interpolators, independent thin-plate spline interpolators, and a Gaussian process outer product emulator with a linear mean function and an exponential covariance function separable in latitude and longitude. None produce obviously better emulation than the simple linear emulator, and most suffer from some ‘overshoot’ problems where the emulator failed to capture rapid changes in output near $ECS_{2xC} = 2.7$ K, at which the AMOC collapses (Figure S6). A linear interpolator emulator has the disadvantage of not being able to estimate its own interpolation uncertainty (‘code uncertainty’), but the code uncertainty estimates from the Gaussian process emulator were much smaller than the temperature reconstruction and UVic model errors, and are presumably negligible in the inference.

6.3 Statistical Model

For statistical analysis it is assumed that the temperature anomaly reconstructions are normally distributed about the (emulated) modeled anomalies for some “best” value of ECS_{2xC} , possibly with some bias (b). That is,

$$T_{obs} \sim N(\mu=T_{mod}(ECS_{2xC}) + b, \Sigma), \quad (S2)$$

or, equivalently,

241

242
$$T_{obs} = T_{mod}(ECS_{2xC}) + b + \varepsilon, \varepsilon \sim N(\mu=0, \Sigma) \quad (S3)$$

243

244 where T_{obs} , T_{mod} , b , and ε are vectors of length n , and Σ is an $n \times n$ covariance matrix describing
245 the model and observation errors. The inference problem is to compute a probability density
246 function for ECS_{2xC} conditional on the observations, $p(ECS_{2xC} | T_{obs})$.

247

248 To account for the possibility of different biases and errors over land and ocean (see Residual
249 Analysis), the vectors and matrices are decomposed into separate land and ocean blocks. The
250 bias is then $b = [b_L \ b_O]$ where b_L and b_O are constant vectors of length $n_L = 113$ and $n_O = 322$.
251 (Here and elsewhere the same symbol is used to refer to both a scalar and a constant vector equal
252 elementwise to that scalar.) Conceptually a bias can be attributed to systematic errors in the
253 modeled temperatures, the proxy temperature reconstructions, or both. While the UVic model
254 does have spatial biases in surface temperature, the bias in the LGM-modern temperature
255 anomaly should be reduced if the model makes similar absolute errors in the LGM and modern
256 periods. The reconstructions may contain biases e.g. due to age model errors. Since the LGM
257 corresponds to a temperature minimum in time in most regions age model errors can lead to
258 systematically warmer reconstructions. In the default analysis the bias is assumed to be zero,
259 because it is highly confounded with climate sensitivity, the quantity of interest. Arbitrarily
260 large climate sensitivities (cold LGM temperature anomalies) can be made compatible with the
261 data by introducing a sufficiently large positive model bias, and similarly for arbitrarily small
262 climate sensitivities. We later consider sensitivity tests in which small nonzero biases over land

or ocean are assumed.

The error covariance matrix is decomposed into the sum of three different sources of error: observation (proxy) error, spatially correlated error, and an additional small-scale, spatially independent source of error referred to in geostatistics as a ‘nugget’:

$$\Sigma = \Sigma_{obs} + \Sigma_{spatial} + \Sigma_{nugget} . \quad (S4)$$

The proxy reconstruction errors form a vector σ_{obs} . Assuming the reconstruction errors are spatially independent, the corresponding covariance matrix is diagonal containing the error variances, $\Sigma_{obs} = \text{diag}(\sigma_{obs}^2)$. The reconstruction errors are likely not completely spatially independent, but the proxy error estimates used in this analysis do not include estimates of spatial correlation. With sufficient data and a perfect model it is possible to estimate the spatial correlation from the data-model residuals. However, the model is not perfect and its errors are also spatially correlated. Without knowing the reconstruction or model error *a priori*, there is confounding between the two sources of error and their spatial structures cannot be estimated independently.

The other two error terms (spatial and nugget) are introduced to account for this confounding between observation and model error. The spatial error term represents all the spatial dependence in the total residual errors, including both reconstruction and model spatial error.

The spatial correlation function is assumed to be exponentially decaying in distance,

$$\text{cor}(x_i, x_j) = \exp[-d(x_i, x_j)/\lambda] , \quad (\text{S5})$$

where the function $d(\cdot, \cdot)$ gives the geodesic distance between two points on the Earth's surface, and $\lambda = 2000$ km is a spatial correlation e -folding length scale. Future work could make use of more sophisticated (albeit computationally expensive) approaches for specifying covariance functions on the sphere [Jun and Stein, 2007].

This correlation function is homogeneous and isotropic, assigning the same correlation length scale over land and ocean, and in zonal and meridional directions. These assumptions are only approximately correct; for example, one might expect the correlation length to be longer over ocean than land, or longer within a latitudinal zone than along a longitudinal meridian. The latter expectation could be addressed with a correlation function that is separable in latitude and longitude, with separate correlation lengths for each, but it is unclear how then to properly account for geodesic distances on the sphere while maintaining zonal/meridional anisotropy. In general, it seems difficult to significantly improve upon the assumed correlation function without introducing a highly complex non-separable correlation function, while simultaneously guaranteeing both its well-posed form (positive definite on the sphere) and estimating its structure from limited (< 500) data points.

305 The spatial error magnitudes are assumed to differ over land and ocean, σ_L and σ_O . Together
 306 with the correlation function they give a block spatial covariance matrix [Oliver, 2003],

307

$$308 \quad \Sigma_{spatial} = \begin{bmatrix} \sigma_L^2 c_{LL} & \sigma_L \sigma_O c_{LO} \\ \sigma_L \sigma_O c_{LO}^T & \sigma_O^2 c_{OO} \end{bmatrix}, \quad (S6)$$

309

310 where c_{LL} , c_{OO} , c_{LO} matrix blocks give the exponential correlations between land points and other
 311 land points, ocean points and ocean points, and land and ocean points, respectively.

312

313 The third error term, the nugget, is intended to account for spatially independent errors that are
 314 not explicitly accounted for in the reconstruction error Σ_{obs} . These could represent either
 315 additional reconstruction error in case the calculated errors are overconfident, or sub-grid scale
 316 variability in model error, or some combination of both. The nugget covariance matrix is
 317 diagonal since it is spatially independent, but different nugget variances η_L^2 and η_O^2 over land
 318 and ocean. It is given by $\Sigma_{nugget} = \text{diag}([\eta_L^2 \eta_O^2])$, i.e. with two diagonal blocks that are multiples
 319 (η_L^2 and η_O^2) of the identity matrix.

320

321 6.4 Bayesian Inference

322 The Bayesian procedure for inferring the joint probability distribution of a vector of unknown
 323 parameters θ is to construct the posterior probability distribution

324

325
$$p(\theta | T_{obs}) \propto L(T_{obs} | \theta) p(\theta) , \quad (S7)$$

326

327 where $L(T_{obs} | \theta)$ is the likelihood function giving the probability of observing the data assuming
328 known values of the parameters, and $p(\theta)$ is the prior probability of the parameters. In this case
329 the unknown parameters are taken to be the climate sensitivity as well as the land and ocean
330 spatial errors, $\theta = (ECS_{2xC}, \sigma_L, \sigma_O)$. The correlation length λ , nugget errors η_L and η_O , and
331 biases b_L and b_O are also unknown, but we choose to fix them at assumed values rather than infer
332 them.

333

334 The biases are assumed to be zero for reasons discussed above (confounding with ECS_{2xC}). The
335 correlation length and nuggets are fixed to constant values to avoid confounding with σ_L and σ_O .
336 In general, it is difficult to simultaneously estimate the spatial variance, nugget variance, and
337 correlation length of a Gaussian process from limited data. The assumed values are $\lambda = 2000$
338 km, $\eta_L = 2.5$ K, and $\eta_O = 0.5$ K, chosen from a combination of comparative residual analysis
339 over land and ocean, exploratory variogram analysis, inspection of the likelihood surface at
340 different fixed values, and prior expectations about the range of correlation and the relative
341 amounts of temperature variability between land and ocean. We consider later the effects of
342 varying these assumptions.

343

344 The normal likelihood function is given by a multivariate normal distribution,

345

$$346 \quad L(T_{obs} | ECS, \sigma_L, \sigma_O) = \frac{1}{\sqrt{(2\pi)^n \det \Sigma}} \exp \left[-\frac{1}{2} r^T \Sigma^{-1} r \right], \quad (S8)$$

347

$$348 \quad r = T_{obs} - [T_{mod}(ECS_{2xC}) + b],$$

349

350 where r is the bias-corrected data-model residual vector.

351

352 The prior probabilities of the uncertain parameters are assumed independent of each other. The
 353 prior probabilities on the land and ocean spatial errors are assumed to be Lognormal(log(2.5),
 354 log(2)/2), i.e., their logarithm is normal with mean log(2.5) and standard deviation log(2)/2,
 355 intended to reflect a prior error estimate of 2.5 K uncertain by a factor of 2 (from 1.25 to 5 K).
 356 For climate sensitivity, a bounded uniform prior over the range of modeled ECS_{2xC} values (0.26
 357 to 8.37 K) is assumed for simplicity. While this prior has proven controversial for estimating
 358 climate sensitivity from limited instrumental data [e.g. *Frame et al.*, 2005; *Annan and*
 359 *Hargreaves*, 2011], the inference is presumably less sensitive to the prior in a paleo context with
 360 data collected over longer time scales. Furthermore, we consider an alternate prior that is
 361 bounded uniform on the climate feedback ($\propto 1/ECS_{2xC}$). The resulting inference for ECS_{2xC} (see
 362 Sensitivity Analysis) does not strongly differ between the two priors, and other statistical
 363 assumptions have more influence on the inference. Presumably a prior that uses other
 364 constraints (such as modern instrumental data) would give an inference for ECS_{2xC} which lies
 365 somewhere between the inferences from the uniform ECS_{2xC} and uniform feedback priors, which

have prior means — 4.3 and 1.6 K over these bounds, respectively, assuming a 3.7 W m^{-2} forcing for a CO_2 doubling — that are on the upper and lower ends of the $\text{ECS}_{2\times\text{C}}$ ranges found in other studies [Knutti and Hegerl, 2008].

6.5 Monte Carlo Sampling

Given the posterior probability distribution for the uncertain parameters given by the above likelihood function and priors, the Bayesian inference proceeds by Markov chain Monte Carlo (MCMC) sampling using the Metropolis algorithm. The Metropolis algorithm generates a correlated random walk through parameter space designed so that points in parameter space are visited (sampled) in direct proportion to their calculated posterior probability.

The resulting set of samples from the posterior distribution, the Markov chain, can be used to approximate any quantity of interest (means, quantiles, distributions) by sample statistics (sample means or quantiles, histograms or kernel density estimates). A particular advantage of MCMC method is the ease with which they can compute the marginal distributions of individual parameters from the joint posterior of all uncertain parameters. Theoretically, the marginal distribution of a parameter is obtained by averaging over the uncertainty in all other (‘nuisance’) parameters, e.g., for climate sensitivity,

$$p(\text{ECS} | T_{\text{obs}}) = \iint p(\text{ECS}, \sigma_L, \sigma_O | T_{\text{obs}}) d\sigma_L d\sigma_O . \quad (\text{S9})$$

With MCMC sampling the desired marginal distribution can be obtained by simply constructing

a histogram or density estimate of only the ECS_{2xC} samples in the chain, ‘forgetting’ about the samples of the other parameters.

A two-stage adaptive Metropolis algorithm is employed in all analyses. First a preliminary chain of 20,000 samples is constructed using informed guesses for the starting point in the chain and for the step sizes proposed for the random walk. Then a second chain of 100,000 samples is constructed, starting at the posterior mean of the first chain, and with a multivariate normal proposal distribution approximately proportional to the sample covariance of the first chain [Roberts and Rosenthal, 2009]. This allows the Metropolis algorithm to more efficiently propose moves that are adapted in magnitude and direction to the posterior distribution approximated by the first, possibly poorly converged chain. Only the second, adapted chain is used in further analysis.

The resulting chains appear well converged in graphical diagnostics, have reasonable acceptance rates for proposed moves in the random walk (41% for the default analysis), and have reasonable effective sample sizes (between 6000 and 7000 for the three parameters estimated in the default analysis).

6.6 Joint Posterior

The posterior inferred from the proxy data is given in Figure S13. The marginal distribution for ECS_{2xC} is peaked near the posterior mean of 2.2 K, and is multimodal. This multimodality could be partly due to the non-smooth linear interpolation of the model emulator, but also may reflect

real physical behavior of the model (for example, the collapse of the AMOC near $ECS_{2xC} = 2.7$ K). The estimated spatial errors are around 3.5 K over land and 1.5 K over ocean. The joint posterior shows little correlation (confounding) between ECS_{2xC} and the two spatial error parameters.

7. Sensitivity Tests

A number of experiments are performed to examine the sensitivity of the inference to statistical and physical assumptions. These tests, which are summarized graphically in Figures S14 and S14, are described below. In addition to the tension between land and ocean based estimates of ECS_{2xC} , the inferred ECS_{2xC} distribution has some sensitivity to assumptions about bias, nugget variance, and correlation length, as well as dust forcing and sea level SST corrections. Wind stress forcing narrows the uncertainty range but does not significantly change the mean estimate.

7.1 Land/Ocean

The analysis is applied to only the land or only the ocean data. The ocean-only inference for ECS_{2xC} is similar to the combined inference, with a range of about 1.5 to 3 K, indicating that the ocean data dominate the land data in the inference. The land-only inference supports significantly higher climate sensitivities, roughly similar to the 2 to 4.5 K IPCC range.

7.2 Dust Forcing

In order to account for the uncertainty in dust forcing we have estimated the surface temperature

response to dust forcing using a subset of 11 models with different ECS_{2xC} and performed an additional LGM experiment for each of those models without dust radiative forcing. Assuming a linear response to dust forcing, we interpolated between these simulations to fill in the additional ECS_{2xC} values for which no experiments had been performed (0×Dust). Then we extrapolated (doubled) the surface temperature response to estimate two times larger dust forcing (2×Dust). The results from shown that increasing the dust forcing implies a lower ECS_{2xC} (below 2 K) while eliminating the dust forcing implies a higher ECS_{2xC} (near 3 K).

7.3 Wind Stress Forcing

The UVic model uses prescribed wind stress at the sea surface in order to force the ocean and sea ice model components. In the standard model we use present day wind stress. In order to account for changes in winds at the LGM we applied an anomaly (LGM minus LH) calculated from the coupled ocean-atmosphere general circulation model GENMOM [Alder *et al.*, 2011]. Monthly mean anomalies were added to the seasonal climatology of the wind stress fields.

In both cases the inference with wind stress corrections favors ECS_{2xC} near 2 K, as in the default analysis, but with reduced uncertainty. The AMOC is significantly stronger in models with GENMOM wind stress forcing (Figure S6) in the LGM run than in the LH run, a result that may be inconsistent with deep ocean carbon isotope paleo-data [Curry and Oppo, 2005], indicating possible structural model uncertainty.

449

450 7.4 Sea Level SST Correction

451 The correction of $\Delta\text{SST}_{\text{SL}} = 0.32$ K added to the simulated SST in order to account for the lower
452 sea level during the LGM was estimated by one additional model simulation as described in
453 section 6. The value of 0.32 K is only half of what one would expect from a simple application
454 of a constant lapse rate of 6 K/km. Uncertain model parameters, such as the application of a
455 reduction of the lapse rate in the calculation of outgoing longwave radiation over topography
456 (this parameter is called *rfactor* in the UVic model version 2.8 source code) may be the reason
457 for this deviation and suggest that the model derived value may be uncertain. We address this
458 uncertainty by varying $\Delta\text{SST}_{\text{SL}}$ from 0 to 0.64.

459 Lower $\text{ECS}_{2\text{xC}}$ (below 1.5 K) is favored in the absence of the sea level correction, whereas
460 higher $\text{ECS}_{2\text{xC}}$ (2 to 3 K) is favored by a larger SST correction.

461

462

463 We have performed additional model experiments with the fully coupled ocean-
464 atmosphere general circulation model OSUVic at T42 resolution as described in [Schmittner *et*
465 *al.*, 2011]. For these experiments we used PMIP3 boundary conditions for ice sheets and
466 atmospheric CO_2 and use present day sea level in one experiment and 120 m lower sea level in
467 the other. The differences between these two models therefore quantify the effect of the sea level
468 lowering on SSTs. Because the model is computationally expensive it was integrated only for
469 240 years. Global mean sea surface temperature difference between the two simulations is 0.3 K
470 between model years 200 and 240. Global marine surface air temperatures are $\Delta\text{SAT}_{\text{SL}} = 0.46$ K

warmer.

Inspection of the spatial distribution shows that over 72% of the surface ocean SSTs are between 0.22 and 0.42 K warmer in the simulation with lower sea level, mainly between 40°S and 40°N. At higher latitudes in the North Atlantic and North Pacific the differences are larger and over the Southern Ocean high latitudes and the Arctic they are smaller. These independent results confirm our best estimate of 0.32 K for the global SST sea level correction.

7.5 North Atlantic Data

The North Atlantic region where the effects of an AMOC collapse in the model (Fig. S6) are strongest is excluded from the analysis, as described in the Data-Model Comparison section 5. This favors lower ECS_{2xC} between 1 and 2 K. Inspection of frequency distributions of temperature anomalies, analogous to Fig. S9 but excluding the North Atlantic region, shows that the main peaks increase for the observations and all models, while cold temperature anomalies (below 3 K for the observations and below -2 K, -3.5 K, and -4.5 K for models with ECS_{2xC} equal to 2 K, 3 K, and 4 K, respectively) become less abundant, and the secondary maximum around -3.5 K for model ECS_{2xC}=2 disappears. This way the temperature distributions at low ECS_{2xC} change from bimodal to unimodal and become more similar to the observed distribution when the North Atlantic region is excluded from the comparison, whereas at high ECS_{2xC} the temperature distributions, without this bimodality, are relatively unchanged in shape. We speculate that this causes lower ECS_{2xC} values to receive higher probability weights in the Bayesian analysis. This sensitivity test indicates that North Atlantic cooling is an influential

constraint, favoring higher ECS_{2xC} values. It demonstrates that excluding regions can lead to a biased ECS_{2xC} estimate, a result that emphasizes the importance of good spatial data coverage.

7.6 Statistical Assumptions

Bias: Four experiments assume nonzero bias over land or ocean of ± 0.5 K. The ocean bias has a particularly strong influence, altering the ECS_{2xC} estimate by about 1 K. The influence of ocean bias is larger than the influence of land bias, due to the ocean data's overall influence on the inference.

Nugget Variance: The assumed nugget error of 2.5 K over land and 0.5 K over ocean is changed to zero over land and ocean (no nugget), or to 3.5 K over land or 1.5 K over ocean (large nugget). Eliminating the nugget implies a larger ECS_{2xC} but produces an extremely narrow uncertainty range, suggesting a mis-specified statistical model. Increasing the nugget eliminates ECS_{2xC} below 2 K but otherwise leaves the posterior unchanged.

Spatial correlation: The assumed correlation length scale of 2000 km is changed to 1000 km or 5000 km. The long correlation length eliminates ECS_{2xC} below 2 K; the short correlation length favors low ECS_{2xC} near 1 K.

Observation error: This sensitivity test explores the role of error specification, in particular the influence of model error and spatial auto-correlation. Here the analysis is repeated neglecting

spatial correlation and model error and assuming only spatially independent observation errors. This gives a very narrow ECS_{2xC} distribution peaked near 3.4 K. The extreme sharpness of the distribution indicates a mis-specification of the statistical model (i.e., it is overconfident due to neglecting model error and spatial dependence).

Spatial error: The analysis is performed assuming only spatially correlated errors (land and ocean variances are estimated from the residuals as in the default analysis), neglecting observation error and the nugget error. This gives a sharp ECS_{2xC} mode near 3 K, although with some probability down to 1 K. The sharp peak also suggests mis-specification (i.e., observation and nugget errors are important).

Heavy tailed likelihood: To explore the possibility of non-normally distributed errors, a multivariate Student-t likelihood is used in place of the multivariate normal likelihood. This distribution has 3 degrees of freedom and has a covariance equal to the covariance assumed in the multivariate normal analysis. This slightly favors lower ECS_{2xC} values but otherwise leaves the ECS distribution unchanged.

Climate sensitivity prior: A prior that is uniform on the climate feedback factor F_{2x}/ECS_{2xC} is used instead of the uniform prior on climate sensitivity. This prior favors slightly lower ECS_{2xC} values but leaves the ECS_{2xC} posterior distribution essentially unchanged.

Outliers excluded: Some grid cells have reconstructed temperature anomalies that are as many

as 6 standard deviations away from the (posterior mean) modeled anomalies. To test the sensitivity of the inference to the presence of outliers, grid cells with reconstructed anomalies more than 3 standard deviations away from the $ECS_{2\times C} = 2.51$ K model run are excluded. This criterion excludes 8 grid cells, all land cells in North America. The exclusion of outliers has negligible effect on the inference.

7.7 Other Uncertainties

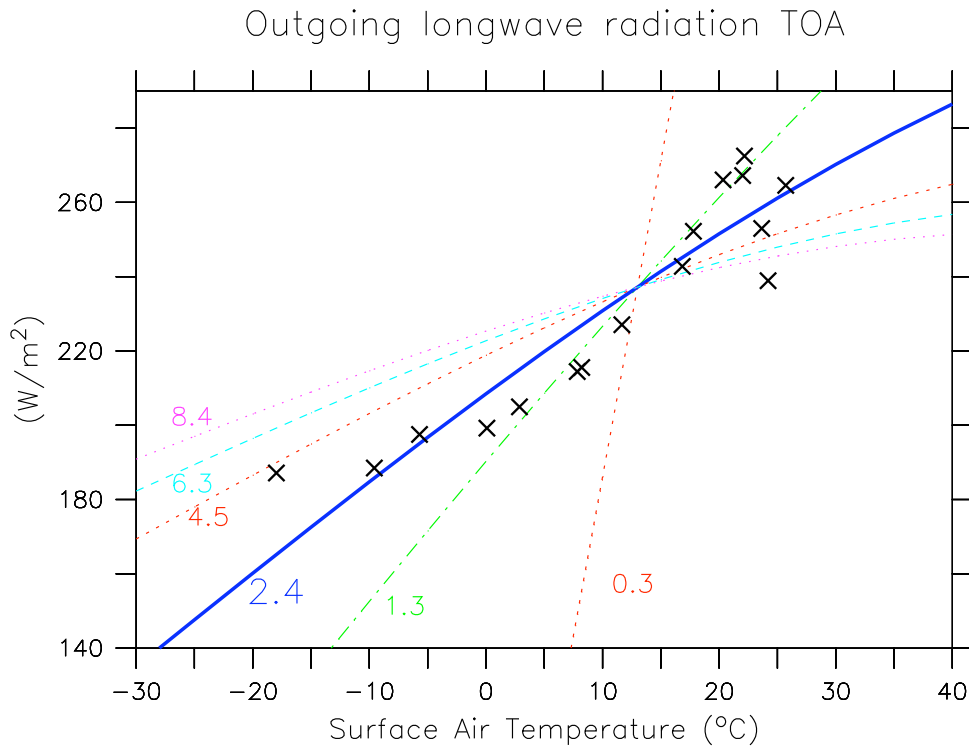
Our study does not provide a complete uncertainty assessment. We have taken into account a number of known important uncertainties such as dust forcing. Others, however, are not included, for example uncertainties in the reconstruction of the ice sheets and vegetation cover. Also our model ensemble does not scan the full parameter space. For example, changes in shortwave radiation due to clouds are not taken into account. Our statistical method does not explicitly consider bias due to limited data coverage.

8. Vegetation Simulation

Our simulations include the influence of climate and atmospheric CO_2 concentrations on the vegetation distribution. Figure S10 shows that the largest changes in simulated vegetation occur at northern hemisphere high latitudes. The simulated dramatic reduction of the boreal/temperate forest in the northern hemisphere extra-tropics from $1.8 \times 10^{-7} \text{ km}^2$ to $0.4 \times 10^{-7} \text{ km}^2$ is consistent with pollen reconstructions and previous offline vegetation modeling [Harrison and Prentice, 2003]. The extent of tropical forest decreases in the model from $2.7 \times 10^{-7} \text{ km}^2$ to $2.4 \times 10^{-7} \text{ km}^2$ is qualitatively consistent with, but quantitatively much less, than simulated by [Harrison and

558 *Prentice, 2003*] who find reductions of $(1.1 \pm 0.3) \times 10^{-7} \text{ km}^2$. Globally the area covered by C_3
 559 grass decreases by 10% (from $4.0 \times 10^{-7} \text{ km}^2$ to $3.6 \times 10^{-7} \text{ km}^2$) whereas C_4 grass coverage
 560 increases by 20% (from $1.1 \times 10^{-7} \text{ km}^2$ to $1.3 \times 10^{-7} \text{ km}^2$) consistent with the competitive advantage
 561 of C_4 photosynthesis under low CO_2 .

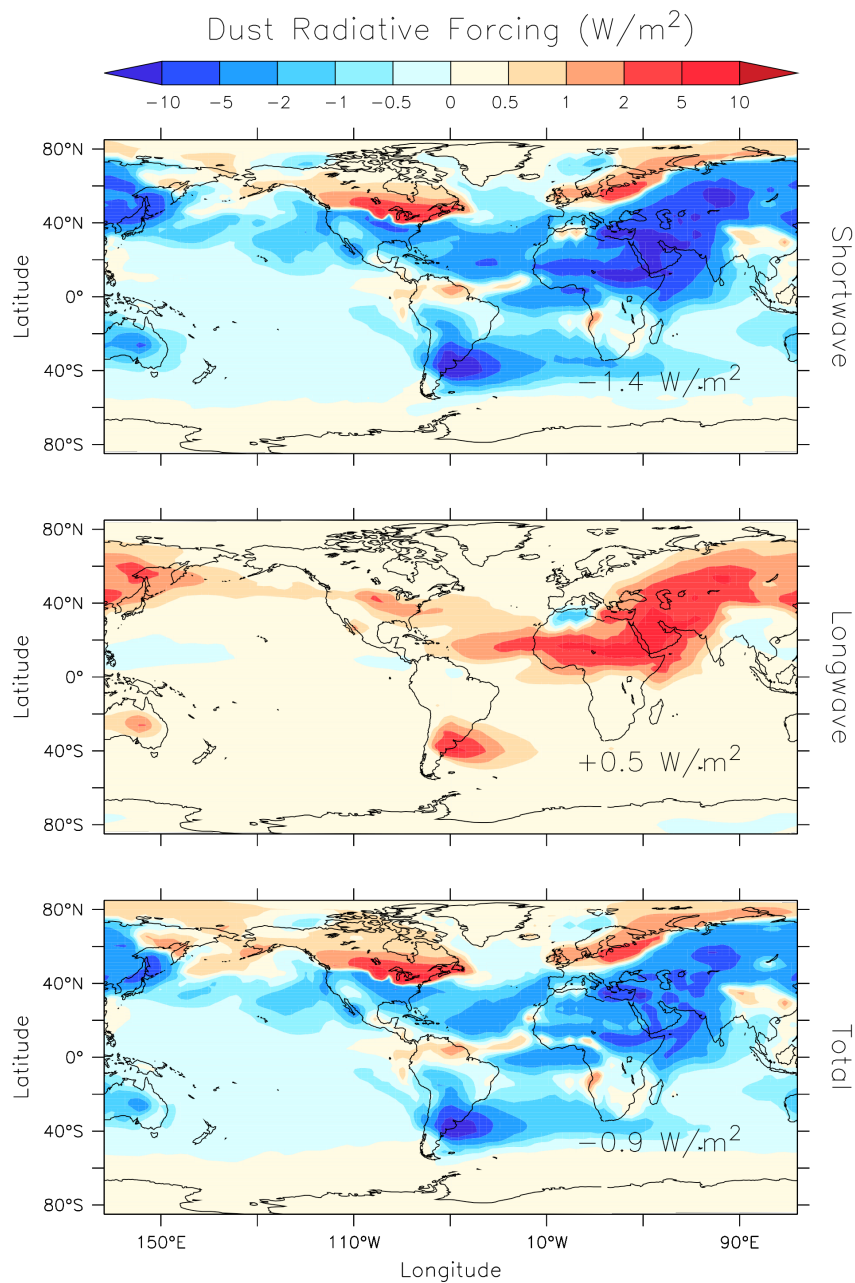
562 Figures



563
 564 Figure S1: Outgoing longwave radiation Q_{PLW} at the top-of-the-atmosphere as a function of
 565 surface air temperature T_a . Colored lines show results of the parameterization by Thompson and
 566 Warren (1982) (equation S1) with different slopes and approximately constant T_a at its
 567 preindustrial value of 13°C . Colored numbers denote the $\text{ECS}_{2\times\text{C}}$ of the different model versions.
 568 Symbols show near-surface (2 m) air temperature data from the NCEP reanalysis [*Kalnay et al.*,
 569 1996] and longwave radiation from ERBE satellite measurements [*Ramanathan et al.*, 1989]

570 averaged over 10 degree latitudinal bands.

571



571

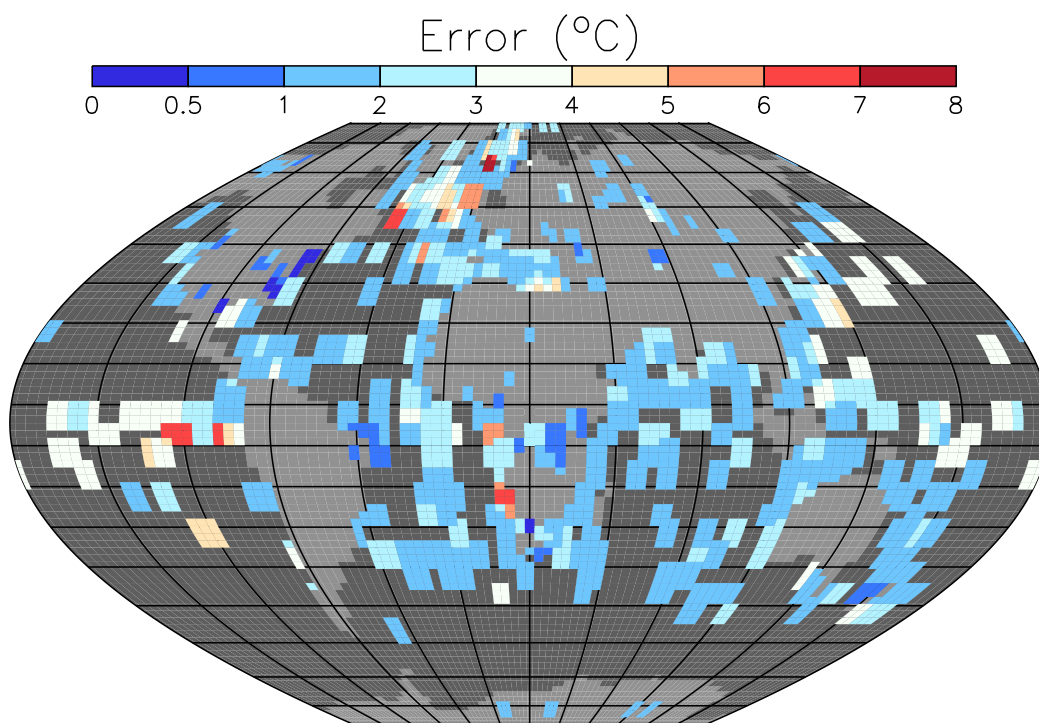
572 Figure S2: Annual mean dust forcing (LGM minus pre-industrial) as a function of longitude and

573 latitude used as a perturbation to the fluxes at the top-of-the-atmosphere in the UVic model. Top:

574 shortwave forcing, center: longwave forcing, bottom: total (shortwave plus longwave) forcing.

575 Negative (blue) values denote a cooling influence, positive (red) a warming. From [Mahowald et

576 al., 2006b].

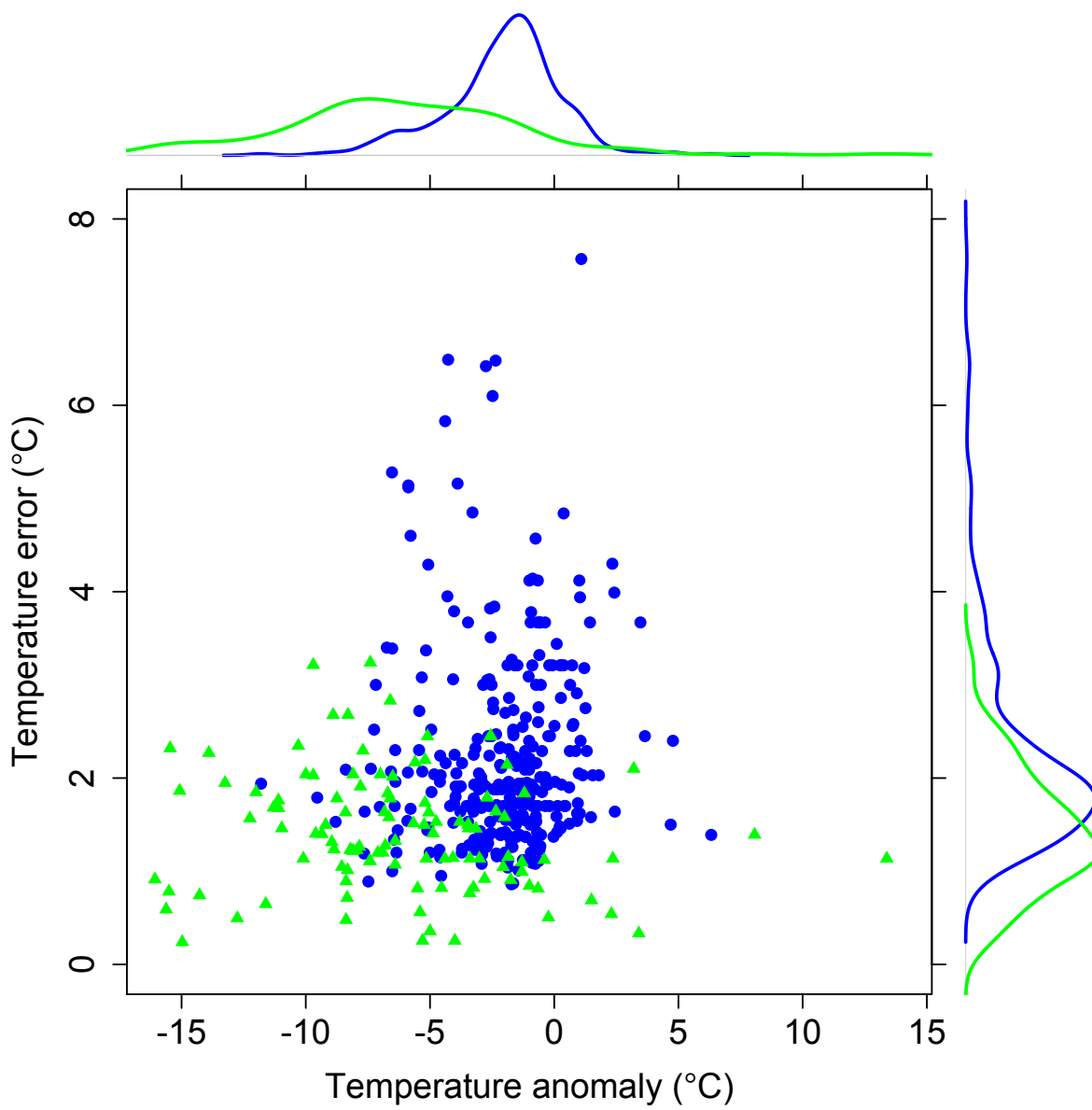


577

578 Figure S3: Error in the LGM temperature reconstructions as reported in the original publications

579 [*MARGO et al.*, 2009; *Bartlein et al.*, 2010; *Shakun et al.*, in review].

580



581

582 Figure S4: Scatterplot of reconstruction error vs. reconstructed temperature anomaly for land
 583 (green) and ocean (blue) data, along with marginal distributions of temperature errors (top) and
 584 temperature anomalies (right).

585

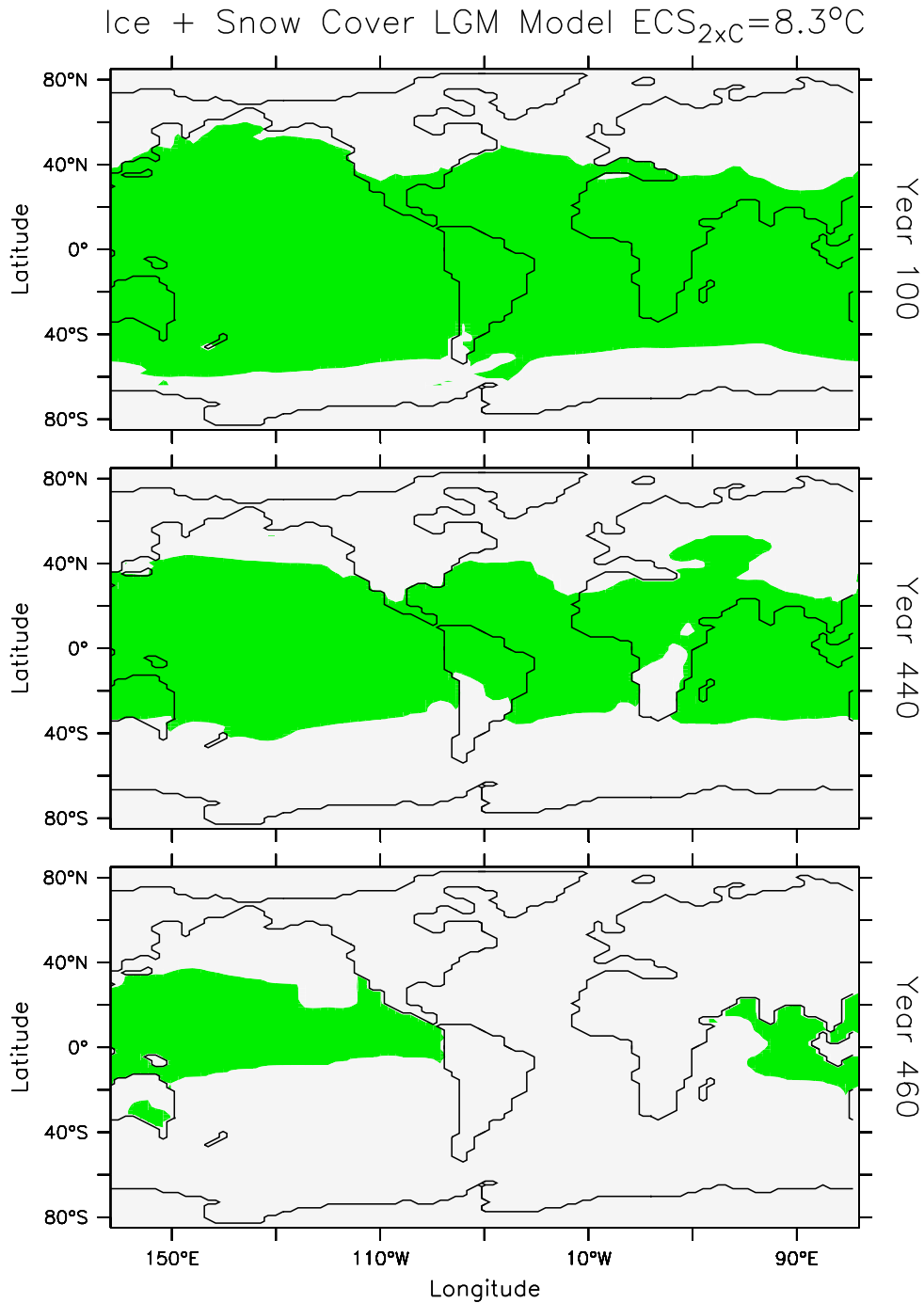
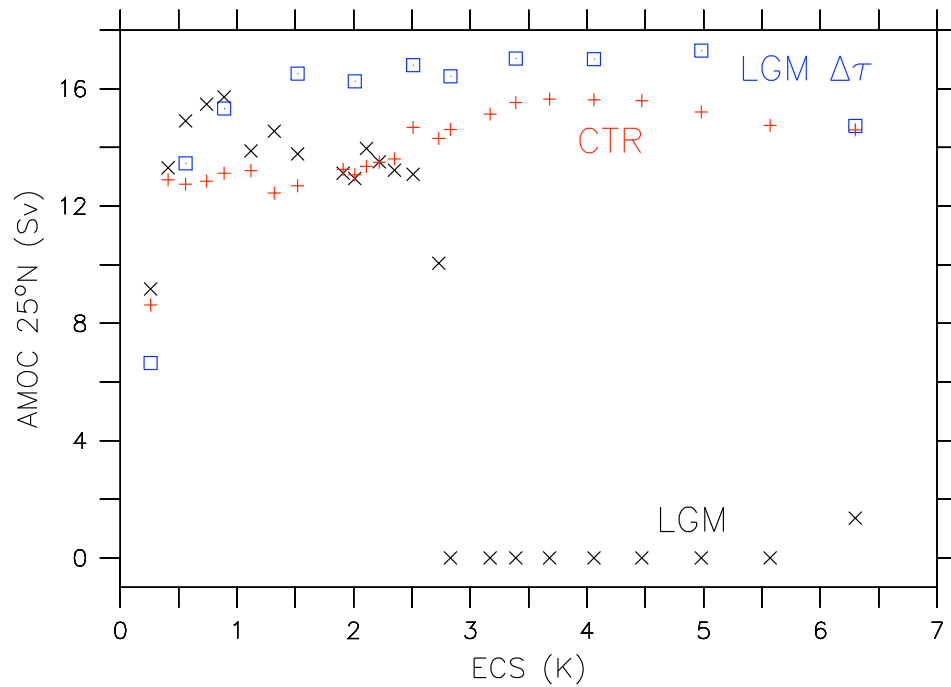


Figure S5. Annual mean snow and ice cover (white) in the LGM experiment with a $ECS_{2xC}=8.3$ K at different times during the integration. Top: 100 model years after the switch to LGM boundary conditions, center: 440 years, and bottom: 460 years.



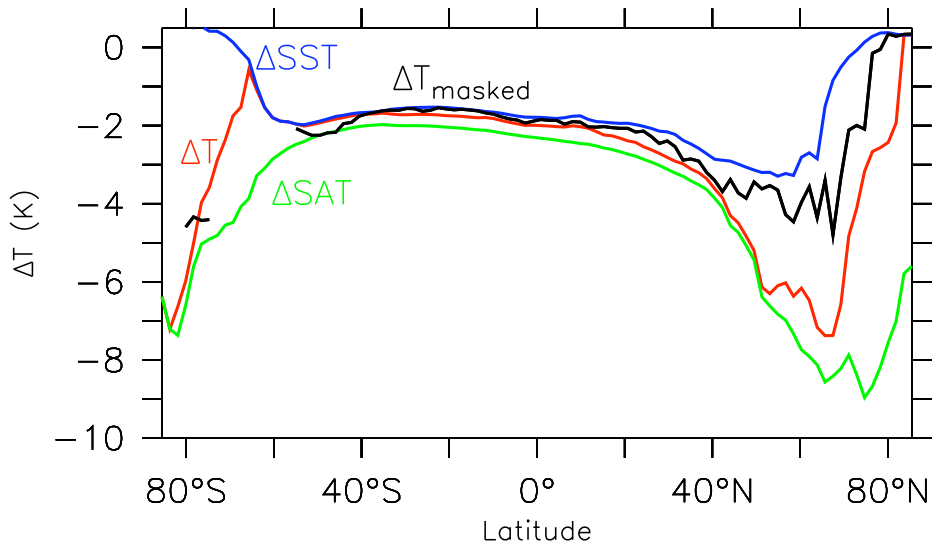
589

590 Figure S6. Simulated Atlantic Meridional Overturning Circulation (AMOC) at 25°N as a
 591 function of the climate sensitivity. Results from the pre-industrial control simulation are shown
 592 as red crosses, LGM results as black xes and results from LGM experiments with wind stress
 593 from GENMOM as blue squares.

594

595

595

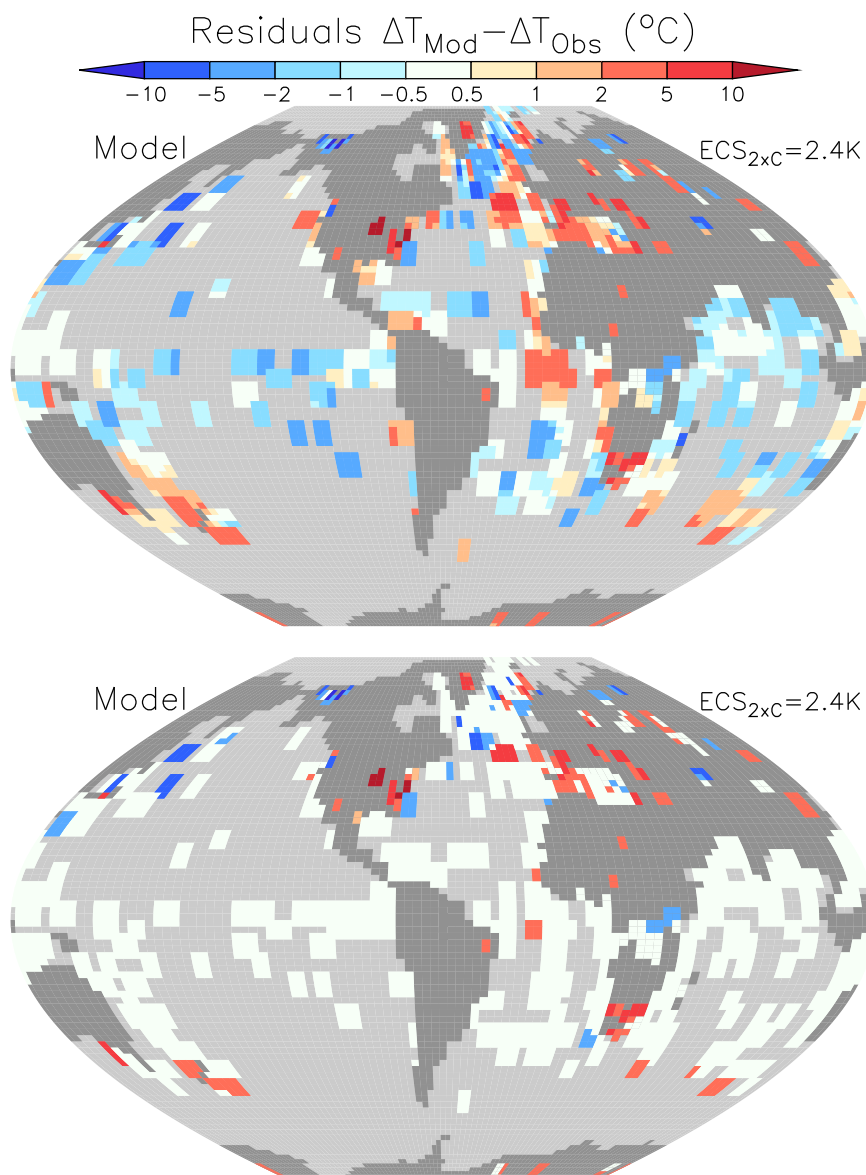


596

597 Figure S7: Zonally averaged surface temperature changes (LGM minus LH) from the best-fitting
 598 model (ECS_{2xC}=2.4 K). Black: surface temperature (SST over the ocean corrected for sea level
 599 lowering by adding 0.3 K, and SAT over land) masked by the grid points that contain
 600 reconstructions. Red: unmasked surface temperature (SST over the ocean and SAT over land).
 601 Green: unmasked SAT. Blue unmasked SST.

602

602



603

604 Figure S8: Residuals (difference in temperature change between model and reconstructions)
 605 from the best fitting model (ECS_{2xC} = 2.4 K) as a function of longitude and latitude. Top panel
 606 shows residuals everywhere, bottom panel only those grid points where the error is outside the
 607 observational error estimates, which accounts for 25% of the global surface area covered by
 608 observations.

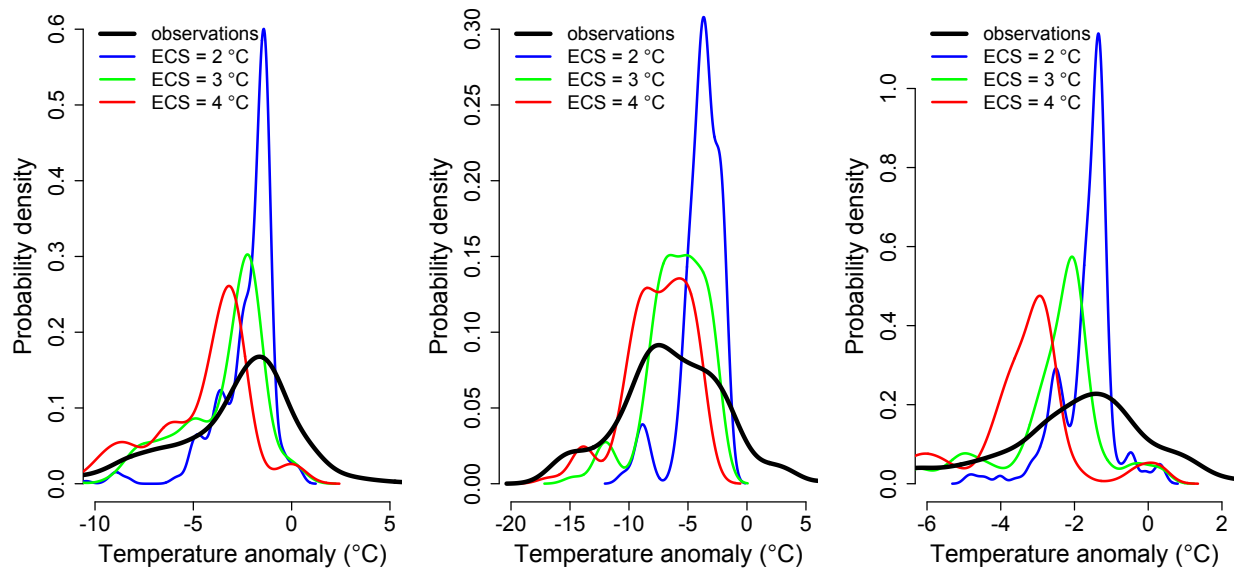


Figure S9: Distributions of reconstructed (observed) and modeled LGM-modern temperature anomalies at selected climate sensitivities, for land and ocean (left), land only (center), and ocean only (right) grid cells.

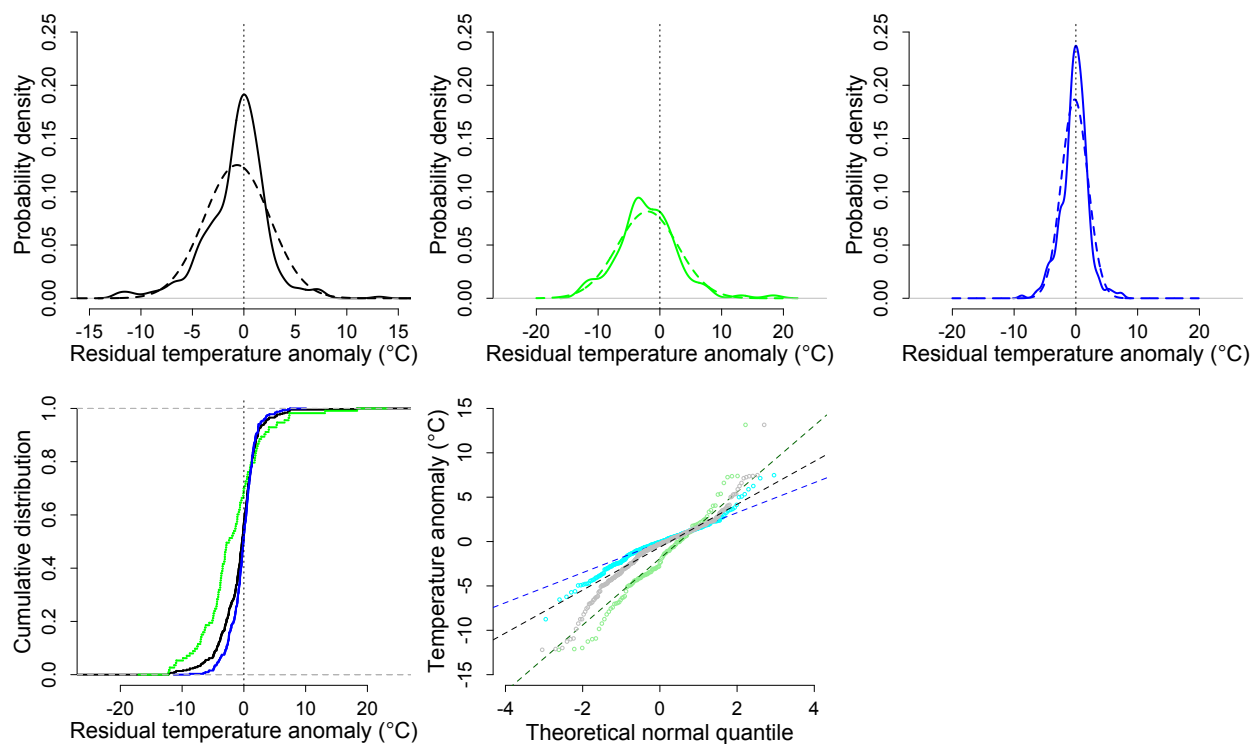
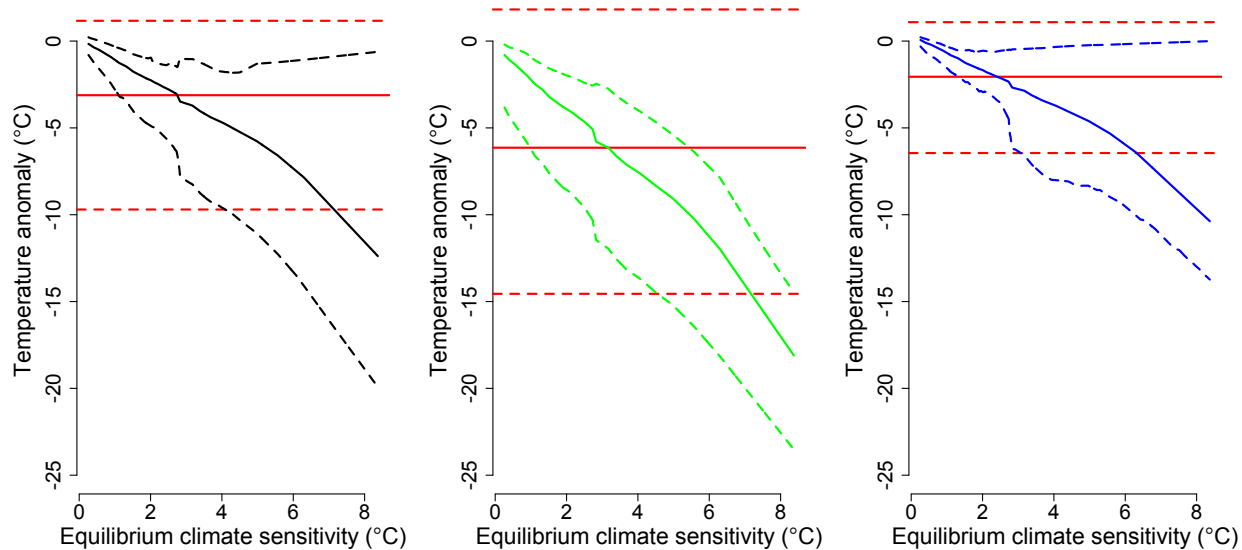
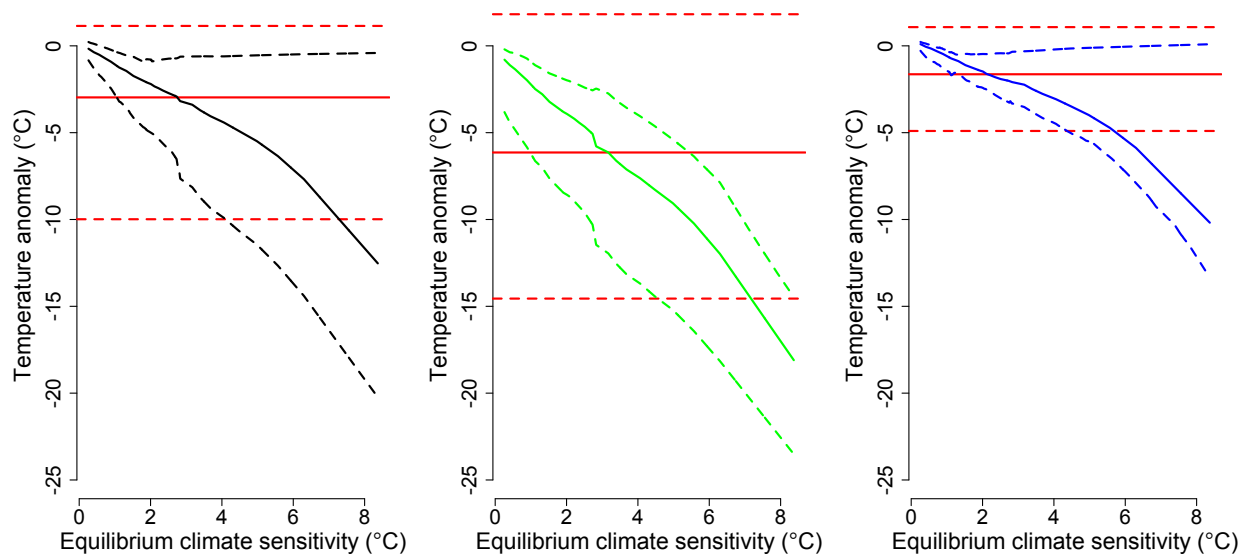


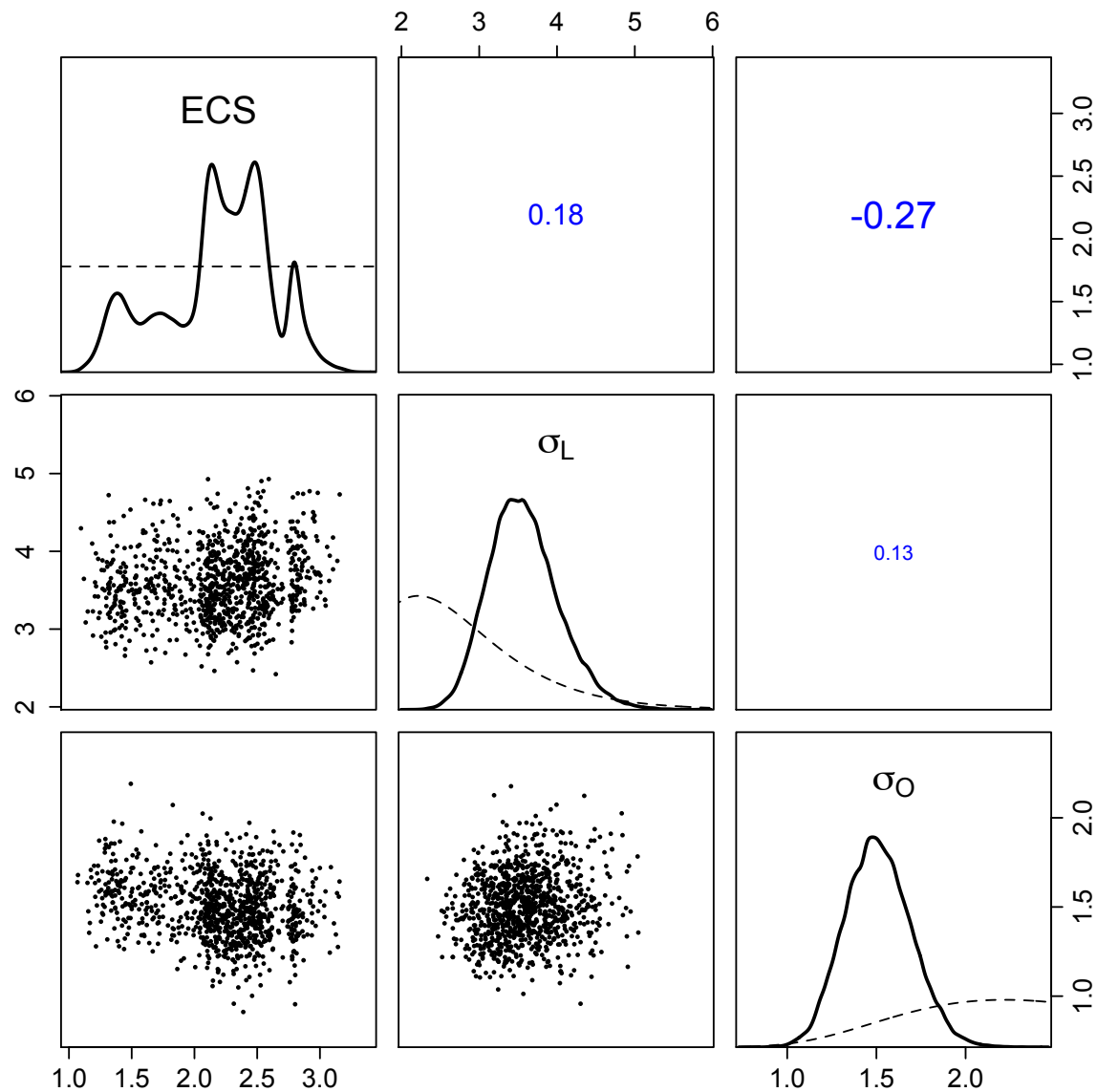
Figure S10: Residuals at the posterior mean climate sensitivity (2.2 K) for land and ocean (upper left), land only (upper center), and ocean only (upper right) grid cells, with normal fits (dashed lines) superimposed. Also shown are cumulative distribution functions of the residuals (lower left) and normal Q-Q plots (lower center) with linear fits between the first and third quartiles (dashed lines).



619
 620 Figure S11: Plot of mean and 90% interval for the reconstructed temperature anomaly (solid and
 621 dashed red lines) and mean and 90% intervals for the modeled temperature anomaly as a
 622 function of ECS_{2xC} for land and ocean (left, black), land only (center, green), and ocean only
 623 (right, blue) grid cells.



624
 625 Figure S12: As in Figure S11, but with grid cells in the North Atlantic region omitted.



626

627 Figure S13: Marginal and pairwise joint posterior distribution of estimated parameters ($ECS_{2 \times C}$,
 628 land spatial error, and ocean spatial error), for the default analysis. The marginal distributions
 629 are given on the diagonal (with priors given by dashed curves), with pairwise scatterplots of
 630 posterior samples given below the diagonal, and pairwise correlations above the diagonals. All
 631 units are in K.

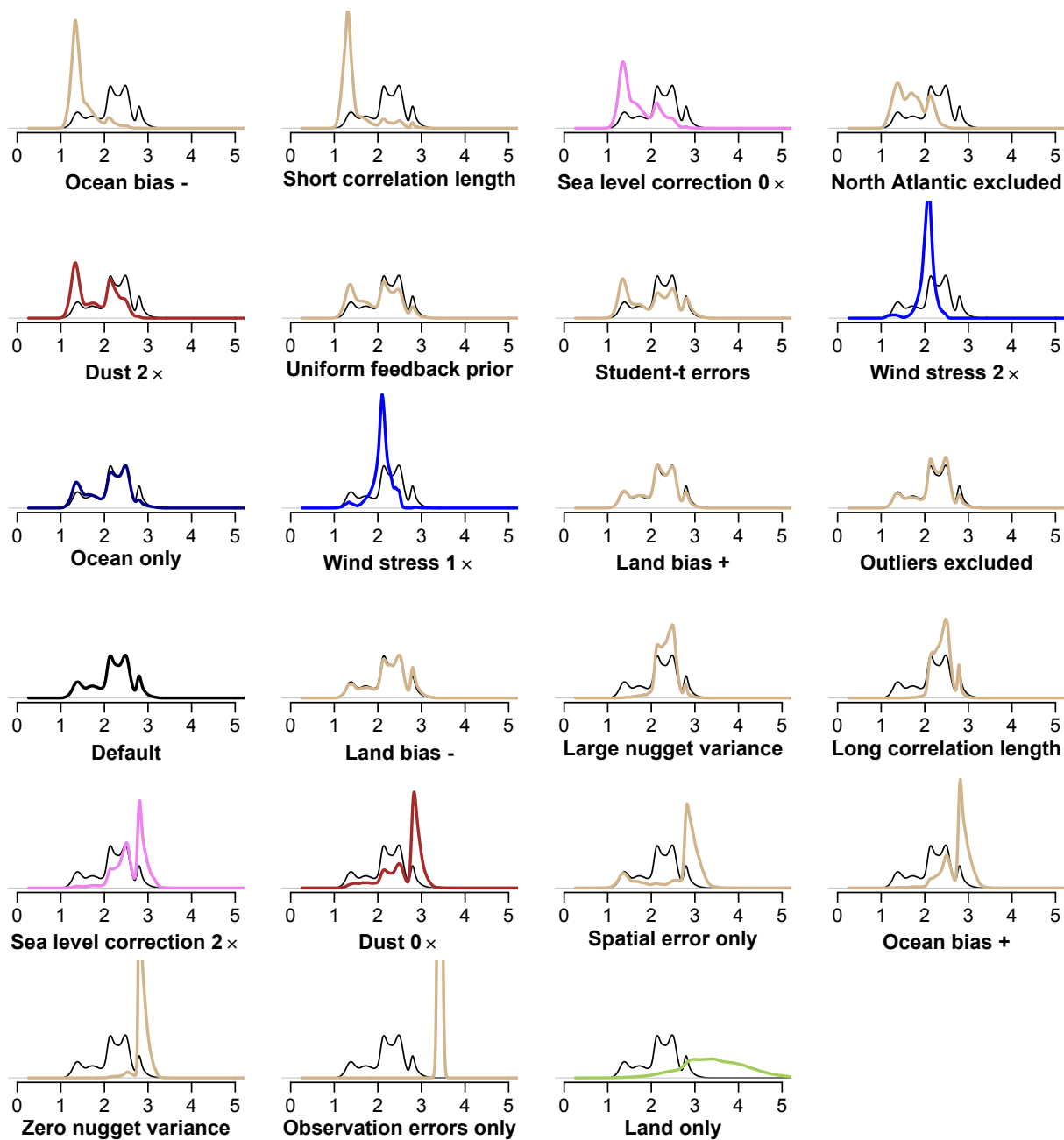
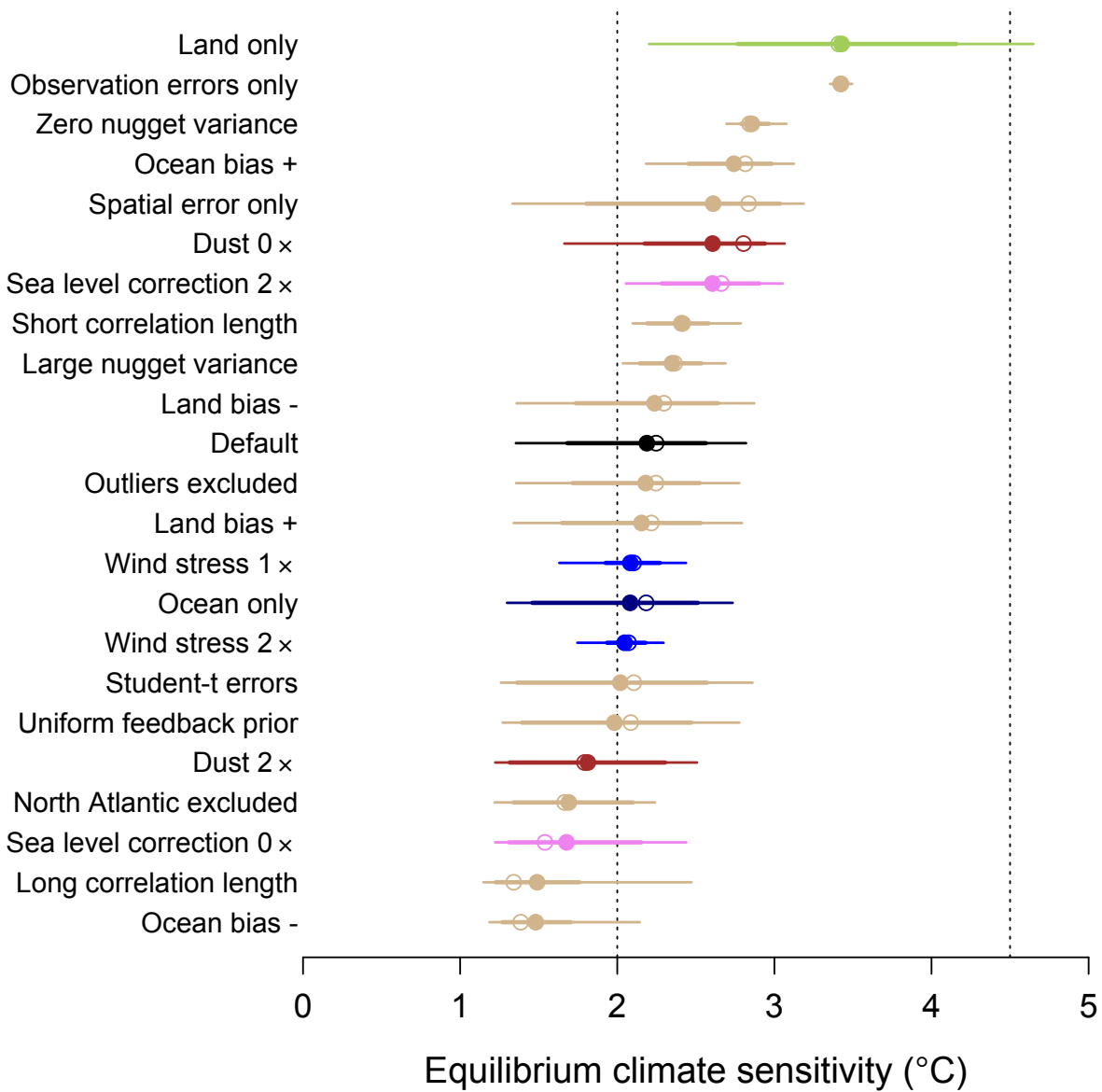
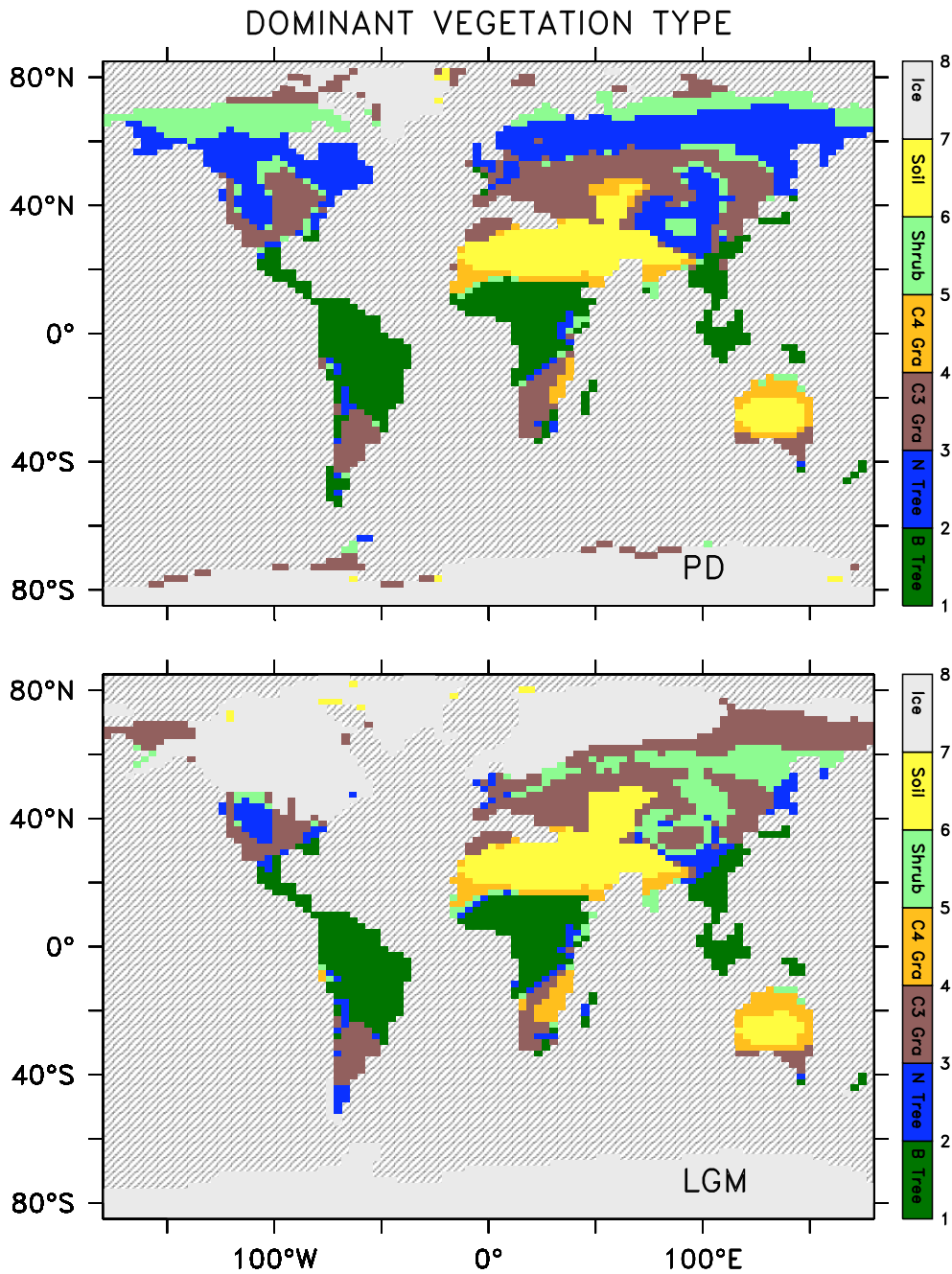


Figure S14: Marginal posterior probability distributions for ECS_{2xC} estimated in each sensitivity experiment (colored curves) compared to the distribution obtained in the default analysis (thin black curve), sorted by increasing mean ECS_{2xC} .



636

637 Figure S15: Mean and median (filled and open circles) ECS_{2xC} values, along with 66% and 90%
 638 intervals (thick and thin lines) for the various sensitivity experiments (as in Figure S14), sorted
 639 by decreasing mean ECS_{2xC}. The vertical dotted lines are the IPCC range of 2–4.5 K.



640

641 Figure S16: Simulation of dominant vegetation type for the present day (top) and the LGM
 642 (bottom) in model ECS_{2xC} = 2.6 K. Five different plant functional types are simulated: broadleaf
 643 trees (green), needleleaf trees (blue), C₃ grass (brown), C₄ grass (orange), and shrub (light green)
 644 in addition to bare soil (yellow).

645

646

References

647

- 648 Alder, J. R., S. W. Hostetler, D. Pollard, and A. Schmittner (2011), Evaluation of a present-day
 649 climate simulation with a new coupled atmosphere-ocean model GENMOM, *Geosci.*
 650 *Model Dev.*, 4(1), 69-83, doi:10.5194/gmd-4-69-2011.
- 651 Annan, J. D., and J. C. Hargreaves (2011), On the generation and interpretation of probabilistic
 652 estimates of climate sensitivity, *Climatic Change*, 104(3-4), 423-436, 10.1007/s10584-
 653 009-9715-y.
- 654 Arbuszewski, J., P. deMenocal, A. Kaplan, and E. C. Farmer (2010), On the fidelity of shell-
 655 derived delta O-18(seawater) estimates, *Earth Planet Sc Lett*, 300(3-4), 185-196, Doi
 656 10.1016/J.Epsl.2010.10.035.
- 657 Bartlein, P., S. Harrison, S. Brewer, S. Connor, B. Davis, K. Gajewski, J. Guiot, T. Harrison-
 658 Prentice, A. Henderson, O. Peyron, I. Prentice, M. Scholze, H. Seppä, B. Shuman, S.
 659 Sugita, R. Thompson, A. Viau, J. Williams, and H. Wu (2010), Pollen-based continental
 660 climate reconstructions at 6 and 21 ka: a global synthesis, *Clim Dynam*, 1-28,
 661 10.1007/s00382-010-0904-1.
- 662 Bartlein, P., S. Harrison, S. Brewer, S. Connor, B. Davis, K. Gajewski, J. Guiot, T. Harrison-
 663 Prentice, A. Henderson, O. Peyron, I. Prentice, M. Scholze, H. Seppä, B. Shuman, S.
 664 Sugita, R. Thompson, A. Viau, J. Williams, and H. Wu (2011), Pollen-based continental
 665 climate reconstructions at 6 and 21 ka: a global synthesis, *Clim Dynam*, 37, 775-802,
 666 10.1007/s00382-010-0904-1.
- 667 Broccoli, A. J. (2000), Tropical cooling at the last glacial maximum: An atmosphere-mixed layer
 668 ocean model simulation, *J Climate*, 13(5), 951-976.
- 669 Curry, W. B., and D. W. Oppo (2005), Glacial water mass geometry and the distribution of delta
 670 C-13 of Sigma CO2 in the western Atlantic Ocean, *Paleoceanography*, 20(1), -.
- 671 EPICA, c. m., L. Augustin, C. Barbante, P. R. F. Barnes, J. M. Barnola, M. Bigler, E. Castellano,
 672 O. Cattani, J. Chappellaz, D. DahlJensen, B. Delmonte, G. Dreyfus, G. Durand, S.
 673 Falourd, H. Fischer, J. Fluckiger, M. E. Hansson, P. Huybrechts, R. Jugie, S. J. Johnsen,
 674 J. Jouzel, P. Kaufmann, J. Kipfstuhl, F. Lambert, V. Y. Lipenkov, G. V. C. Littot, A.
 675 Longinelli, R. Lorrain, V. Maggi, V. Masson-Delmotte, H. Miller, R. Mulvaney, J.
 676 Oerlemans, H. Oerter, G. Orombelli, F. Parrenin, D. A. Peel, J. R. Petit, D. Raynaud, C.
 677 Ritz, U. Ruth, J. Schwander, U. Siegenthaler, R. Souchez, B. Stauffer, J. P. Steffensen, B.
 678 Stenni, T. F. Stocker, I. E. Tabacco, R. Udisti, R. S. W. van de Wal, M. van den Broeke,
 679 J. Weiss, F. Wilhelms, J. G. Winther, E. W. Wolff, and M. Zucchelli (2004), Eight glacial
 680 cycles from an Antarctic ice core, *Nature*, 429(6992), 623-628, Doi
 681 10.1038/Nature02599.
- 682 Flückiger, J., A. Dallenbach, T. Blunier, B. Stauffer, T. F. Stocker, D. Raynaud, and J. M.

683 Barnola (1999), Variations in atmospheric N₂O concentration during abrupt climatic
684 changes, *Science*, 285(5425), 227-230.

685 Frame, D. J., B. B. Booth, J. A. Kettleborough, D. A. Stainforth, J. M. Gregory, M. Collins,
686 and M. R. Allen (2005), Constraining climate forecasts: The role of prior assumptions,
687 *Geophys Res Lett*, 32(9), L09702, doi:10.1029/2004gl022241.

688 Hansen, J., A. Lacis, D. Rind, G. Russell, P. Stone, I. Fung, R. Ruedy, and J. Lerner (1984),
689 Climate sensitivity: Analysis of feedback mechanisms, in *Climate Processes and Climate*
690 *Sensitivity*, edited by J. E. Hansen and T. Takahashi, pp. 130-163, American Geophysical
691 Union.

692 Harrison, S. P., and I. C. Prentice (2003), Climate and CO₂ controls on global vegetation
693 distribution at the last glacial maximum: analysis based on palaeovegetation data, biome
694 modelling and palaeoclimate simulations, *Global Change Biol*, 9(7), 983-1004.

695 Hewitt, C. D., and J. F. B. Mitchell (1997), Radiative forcing and response of a GCM to ice age
696 boundary conditions: cloud feedback and climate sensitivity, *Clim Dynam*, 13(11), 821-
697 834.

698 Jun, M., and M. L. Stein (2007), An approach to producing space - Time covariance functions on
699 spheres, *Technometrics*, 49(4), 468-479, 10.1198/004017007000000155.

700 Kalnay, E., M. Kanamitsu, R. Kistler, W. Collins, D. Deaven, L. Gandin, M. Iredell, S. Saha, G.
701 White, J. Woollen, Y. Zhu, M. Chelliah, W. Ebisuzaki, W. Higgins, J. Janowiak, K. C.
702 Mo, C. Ropelewski, J. Wang, A. Leetmaa, R. Reynolds, R. Jenne, and D. Joseph (1996),
703 The NCEP/NCAR 40-year reanalysis project, *B Am Meteorol Soc*, 77(3), 437-471.

704 Knutti, R., and G. C. Hegerl (2008), The equilibrium sensitivity of the Earth's temperature to
705 radiation changes, *Nat Geosci*, 1(11), 735-743.

706 Köhler, P., R. Bintanja, H. Fischer, F. Joos, R. Knutti, G. Lohmann, and V. Masson-Delmotte
707 (2010), What caused Earth's temperature variations during the last 800,000 years? Data-
708 based evidence on radiative forcing and constraints on climate sensitivity, *Quaternary Sci*
709 *Rev*, 29(1-2), 129-145, [Doi 10.1016/J.Quascirev.2009.09.026](https://doi.org/10.1016/j.quascirev.2009.09.026).

710 Mahowald, N. M., D. R. Muhs, S. Levis, P. J. Rasch, M. Yoshioka, C. S. Zender, and C. Luo
711 (2006a), Change in atmospheric mineral aerosols in response to climate: Last glacial
712 period, preindustrial, modern, and doubled carbon dioxide climates, *Journal of*
713 *Geophysical Research-Atmospheres*, 111(D10), D10202, doi:10.1029/2005jd006653.

714 Mahowald, N. M., M. Yoshioka, W. D. Collins, A. J. Conley, D. W. Fillmore, and D. B.
715 Coleman (2006b), Climate response and radiative forcing from mineral aerosols during
716 the last glacial maximum, pre-industrial, current and doubled-carbon dioxide climates,
717 *Geophys Res Lett*, 33, L20705, 10.1029/2006GL026126.

718 MARGO, C. Waelbroeck, A. Paul, M. Kucera, A. Rosell-Melee, M. Weinelt, R. Schneider, A. C.
719 Mix, A. Abelmann, L. Armand, E. Bard, S. Barker, T. T. Barrows, H. Benway, I. Cacho,
720 M. T. Chen, E. Cortijo, X. Crosta, A. de Vernal, T. Dokken, J. Duprat, H. Elderfield, F.
721 Eynaud, R. Gersonde, A. Hayes, M. Henry, C. Hillaire-Marcel, C. C. Huang, E. Jansen,
722 S. Juggins, N. Kallel, T. Kiefer, M. Kienast, L. Labeyrie, H. Leclaire, L. Londeix, S.
723 Mangin, J. Matthiessen, F. Marret, M. Meland, A. E. Morey, S. Mulitza, U. Pflaumann,

- N. G. Pisias, T. Radi, A. Rochon, E. J. Rohling, L. Sbaffi, C. Schafer-Neth, S. Solignac, H. Spero, K. Tachikawa, and J. L. Turon (2009), Constraints on the magnitude and patterns of ocean cooling at the Last Glacial Maximum, *Nat Geosci*, 2(2), 127-132, [Doi 10.1038/Ngeo411](https://doi.org/10.1038/Ngeo411).
- Mathien-Blard, E., and F. Bassinot (2009), Salinity bias on the foraminifera Mg/Ca thermometry: Correction procedure and implications for past ocean hydrographic reconstructions, *Geochem Geophys Geosy*, 10, Q12011, [Doi 10.1029/2008gc002353](https://doi.org/10.1029/2008gc002353).
- Oliver, D. S. (2003), Gaussian cosimulation: Modelling of the cross-covariance, *Mathematical Geology*, 35(6), 681-698.
- Peltier, W. R. (2004), Global Glacial Isostasy and the Surface of the Ice-Age Earth: The ICE-5G (VM2) Model and GRACE, *Annual Review of Planetary Sciences*, 32, 111-149, [10.1146/annurev.earth.32.082503.144359](https://doi.org/10.1146/annurev.earth.32.082503.144359).
- Perlwitz, J., I. Tegen, and R. L. Miller (2001), Interactive soil dust aerosol model in the GISS GCM 1. Sensitivity of the soil dust cycle to radiative properties of soil dust aerosols, *Journal of Geophysical Research-Atmospheres*, 106(D16), 18167-18192.
- Ramanathan, V., R. D. Cess, E. F. Harrison, P. Minnis, B. R. Barkstrom, E. Ahmad, and D. Hartmann (1989), Cloud-Radiative Forcing and Climate - Results from the Earth Radiation Budget Experiment, *Science*, 243(4887), 57-63.
- Ramaswamy, V., O. Boucher, J. Haigh, D. Hauglustaine, J. Haywood, G. Myhre, T. Nakajima, G. Y. Shi, and S. Solomon (2001), Radiative Forcing of Climate Change, in *Climate Change 2001: The Scientific Basis. Contribution of Working Group I to the Third Assessment Report of the Intergovernmental Panel on Climate Change*, edited by J. T. Houghton, et al., p. 881, Cambridge University Press, Cambridge, United Kingdom, New York, NY, USA.
- Roberts, G. O., and J. S. Rosenthal (2009), Examples of Adaptive MCMC, *Journal of Computational and Graphical Statistics*, 18(2), 349-367, [10.1198/jcgs.2009.06134](https://doi.org/10.1198/jcgs.2009.06134).
- Saenko, O. A., A. Schmittner, and A. J. Weaver (2004), The Atlantic-Pacific seesaw, *J Climate*, 17(11), 2033-2038.
- Schmittner, A., A. Oschlies, H. D. Matthews, and E. D. Galbraith (2008), Future changes in climate, ocean circulation, ecosystems, and biogeochemical cycling simulated for a business-as-usual CO2 emission scenario until year 4000 AD, *Global Biogeochem Cy*, 22(1), GB1013, [Doi 10.1029/2007gb002953](https://doi.org/10.1029/2007gb002953).
- Schmittner, A., T. A. Silva, K. Fraedrich, E. Kirk, and F. Lunkeit (2011), Effects of mountains and ice sheets on global ocean circulation, *J Climate*, 24, 2814-2829, [doi:10.1175/2010JCLI3982.1](https://doi.org/10.1175/2010JCLI3982.1).
- Shakun, J. D., P. U. Clark, F. He, Z. Liu, B. Otto-Bliesner, S. A. Marcott, A. C. Mix, A. Schmittner, and E. Bard (2011), Influence of CO2 and ocean circulation on global climate during the last deglaciation, *Nature*, in review.
- Shakun, J. D., P. U. Clark, F. He, Z. Liu, B. Otto-Bliesner, S. A. Marcott, A. C. Mix, A. Schmittner, and E. Bard (in review), CO2 forcing of climate during the last deglaciation.
- Sokolik, I. N., and O. B. Toon (1999), Incorporation of mineralogical composition into models

- of the radiative properties of mineral aerosol from UV to IR wavelengths, *Journal of Geophysical Research-Atmospheres*, 104(D8), 9423-9444.
- Taylor, K. E., M. Crucifix, P. Braconnot, C. D. Hewitt, C. Doutriaux, A. J. Broccoli, J. F. B. Mitchell, and M. J. Webb (2007), Estimating shortwave radiative forcing and response in climate models, *J Climate*, 20(11), 2530-2543, Doi 10.1175/Jcli4143.1.
- Weaver, A. J., M. Eby, E. C. Wiebe, C. M. Bitz, P. B. Duffy, T. L. Ewen, A. F. Fanning, M. M. Holland, A. MacFadyen, H. D. Matthews, K. J. Meissner, O. Saenko, A. Schmittner, H. X. Wang, and M. Yoshimori (2001), The UVic Earth System Climate Model: Model description, climatology, and applications to past, present and future climates, *Atmos Ocean*, 39(4), 361-428.
- Yoshioka, M., N. M. Mahowald, A. J. Conley, W. D. Collins, D. W. Fillmore, C. S. Zender, and D. B. Coleman (2007), Impact of desert dust radiative forcing on Sahel precipitation: Relative importance of dust compared to sea surface temperature variations, vegetation changes, and greenhouse gas warming, *J Climate*, 20(8), 1445-1467, Doi 10.1175/Jcli4056.1.